Supporting Information

Experimental Section

Materials: Hydrated cobalt chloride (CoCl$_2$•6H$_2$O; ≥ 98%), hydrated trisodium citrate (soft mold i.e. Na$_3$C$_6$H$_5$O$_7$•2H$_2$O; ≥ 99%), sodium thiosulfate (Na$_2$S$_2$O$_3$; ≥ 98%), urea (CN$_2$H$_4$O, 99.0%), and sodium sulfide nonahydrate (NaS$_2$•9H$_2$O, 98.0%) were purchased from Alfa-Aesar and directly used without purification. The carbon cloth was purchased from Japan Toray Company. Sodium nitrate (NaNO$_3$, 99.0%), sodium nitrite (NaNO$_2$, 99.0%), ammonium chloride (NH$_4$Cl), sodium hydroxide (NaOH), potassium hydroxide (KOH), sodium salicylate (C$_7$H$_5$NaO$_3$), trisodium citrate dihydrate (C$_6$H$_5$Na$_3$O$_7$·2H$_2$O), p-dimethylaminobenzaldehyde (C$_9$H$_{11}$NO), sodium nitroferricyanide dihydrate (Na$_2$Fe(CN)$_5$NO·2H$_2$O), 0.8wt% sulfamic acid solution (H$_3$NO$_3$S), sodium dihydrogen phosphate dihydrate (NaH$_2$PO$_4$), disodium hydrogen phosphate dodecahydrate (Na$_2$HPO$_4$) and sodium hypochlorite solution (NaClO) were purchased from Aladdin Ltd. (Shanghai, China). Ultrapure water used throughout all experiments was purified through a Millipore system.

Synthesis of carbon paper @ CoS$_2$ octahedron: In a typical synthesis, Na$_3$C$_6$H$_5$O$_7$·2H$_2$O (1 mmol), CoCl$_2$•6H$_2$O (0.5 mmol) and Na$_2$S$_2$O$_3$ (5 mmol) were dissolved in 75 mL of deionized water and stirred for 20 min to form a clear solution. A piece of a carbon paper (4 cm × 1.5 cm) was annealed in air and carefully cleaned in an ultrasound bath with ethanol and DI water for 10 min each. The aqueous solution and the carbon paper were transferred to a Teflon-lined stainless-steel autoclave (100 mL) and maintained at 200° C for 12 h, and then cooled down to room temperature. The samples were rinsed several times with deionized water and ethanol with the assistance of ultrasonication, and dried at 80 ° C for 8 h.

Synthesis of carbon paper @ CoS$_2$ array: In a typical reaction, CoCl$_2$·6H$_2$O (3 mmol)

and CN_2H_4O (18 mmol) were dissolved in 60 mL of deionized water and stirred for 20 min to form a clear solution. A piece of a carbon paper (4 cm × 1.5 cm) was annealed in air and carefully cleaned in an ultrasound bath with ethanol and DI water for 10 min each. The aqueous solution and the carbon paper were transferred to a Teflon-lined stainless-steel autoclave (100 mL) and maintained at 120° C for 8 h, and then cooled down to room temperature. The precursor sample was rinsed several times with deionized water and ethanol with the assistance of ultrasonication, and dried at 80 ° C for 8 h. Then, 10 mM $NaS_2 \cdot 9H_2O$ was dissolved in 60 mL of deionized water and stirred for 20 min to form a clear solution. The aqueous solution and the precursor sample were transferred to a PPL lined hydrothermal autoclave (100 ml) and maintained at 220° C for 24 h. The samples were rinsed several times with deionized water and ethanol with the assistance of ultrasonication, and dried at 80 ° C for 8 h.

Characterizations: The crystallinity and composition of the synthesized samples were characterized by X-ray diffraction (XRD; Rigaku Co.) with Cu Kα radiation ($\lambda = 1.5406$ Å) and X-ray photoelectron spectroscopy (XPS; ESCALAB250Xi, Thermo Fisher Scientific). The morphological features and detailed structural information were conducted by field-emission scanning electron microscopy (FESEM; GeminiSEM, Zeiss), and transmission electron microscopy (TEM; JEOL JEM-2100F). High-angle annular dark-field scanning transmission electron microscopy (HAADF-STEM) was carried out using a JEOL JEMARM200F STEM/TEM (resolution of 0.08 nm). The absorbance data of spectrophotometer were acquired on SHIMADZU UV-1800 UV-Vis spectrophotometer.

Electrochemical measurements: NO_3^- reduction experiments were carried out in a

two-compartment cell under ambient condition, which was separated by Nafion 117 membrane. The membrane was protonated by first boiling in ultrapure water for 1 h and treating in H_2O_2 (5 wt%) aqueous solution at 80 °C for another 1 h, respectively. And then, the membrane was treaded in 0.5 M H_2SO_4 for 3 h at 80 °C and finally in water for 6 h. The electrochemical experiments were carried out with an electrochemical workstation (CHI 660E) using a three-electrode configuration with prepared electrodes, graphite rod and Ag/AgCl electrode (saturated KCl electrolyte) as working electrode, counter electrode and reference electrode, respectively. The potentials reported in this work were converted to reversible hydrogen electrode (RHE) scale via calibration with the following equation: E (vs. RHE) = E (vs. Ag/AgCl) + 0.059 × pH + 0.197 V and the presented current density was normalized to the geometric surface area. For electrochemical NO_3^- reduction, chrono-amperometry tests were conducted in 1 M KOH solution with 0.1 M NO_3^-.

Determination of NH$_3$: Owing to the large concentration of solution, the obtained reaction solutions were diluted 100 times. Specifically, 4 mL electrolyte was obtained from the cathodic chamber and mixed with 50 μL oxidizing solution containing NaClO (ρCl = 4 ~ 4.9) and NaOH (0.75 M), 500 μL coloring solution containing 0.4 M $C_7H_6O_3Na$ and 0.32 M NaOH, and 50 μL catalyst solution (1 wt% $Na_2[Fe(CN)_5NO]$) for 2 h. Absorbance measurements were performed at 654 nm. The concentration-absorbance curve was calibrated using standard NH$_3$ solution with a series of concentrations. The fitting curve (y = 0.313 x + 0.0313, R^2 = 0.999) shows good linear relation of absorbance value with NH$_3$ concentration.

In addition, ^1H NMR spectroscopy (600 MHz) was also used to detect ammonia in the isotope-labelling measurement. The collected NH_3 sample was first diluted to the detection range and adjust to pH 1.0 by adding 0.1 M HCl. Next, 0.5 ml of the sample solution was mixed 0.1ml DMSO-d_6.

Determination of N_2H_4: A mixed solution of 1.97 g $C_9H_{11}NO$, 10 mL concentrated HCl and 100 ml ethanol was used as a color reagent. Calibration curve was plotted as follow: firstly, preparing a series of N_2H_4 solutions of known concentration as standards; secondly, adding 4 mL color reagent to above N_2H_4 solution, separately, and standing 20 min at room temperature; finally, the absorbance of the resulting solution was measured at 460 nm.

Determination of NO_2^-: Owing to the large concentration of solution, the obtained reaction solutions were diluted 20 times. The NO_2^- concentration was analyzed using the Griess test.[1] The Griess reagent was prepared by dissolving 0.1 g N-(1-naphthyl) ethylenediamine dihydrochloride, 1.0 g sulfonamide and 2.94 mL H_3PO_4 in 50 mL deionized water. In a typical colorimetric assay, the 1.0 mL Griess reagent was mixed with the 1.0 mL nitrite-containing solution and 2.0 mL H_2O and allowed to react at room temperature for 10 min, in which sulfonamide reacts with NO_2^- to form a diazonium salt and then further reacts with amine to form an azo dye (magenta). The absorbance at 540 nm was measured to quantify the NO_2^- concentration with a standard curve of NO_2^- (y = 0.53986x + 0.01177, R^2 = 0.999).

Determination of FE and NH_3 yield: The FE for N_2 reduction was defined as the amount of electric charge used for synthesizing NH_3 divided the total charge passed

through the electrodes during the electrolysis. The total amount of NH_3 produced was measured using colorimetric methods. Assuming three electrons were needed to produce one NH_3 molecule, the FE could be calculated as follows:

$$FE = 8 \times F \times [NH_3] \times V / (17 \times Q) \times 100\% \qquad (1)$$

NH_3 yield was calculated using the following equation:

$$NH_3 \text{ yield rate} = [NH_3] \times V / (s \times t) \qquad (2)$$

where F is the Faraday constant, $[NH_3]$ is the measured NH_3 concentration, V is the volume of the electrolyte in the cathodic chamber, Q is the total quantity of applied electricity; t is the reduction time; s is the electrode area.

Electrochemical in-situ Raman spectroscopy measurements: In-situ Raman measurements were carried out on an XploRA PLUS Raman spectrometer (Horiba Jobin Yvon) equipped with a 50×objective and a 638 nm He-Ne laser. All spectra were recorded by using a commercial three-electrode spectro-electrochemical cell (Gaussian-Union Ltd.Co). The as prepared materials, Ag/AgCl (3.0 M KCl), and Pt slice were employed as the working, reference, and counter electrode, respectively. The Ar-saturated 1M KOH with 0.1 M $NaNO_3$ was used as electrolyte. The signal acquisition duration was 10 s and the filter was 20%.

Electrochemical ATR-FTIR spectroscopy measurements: The in situ electrochemical ATR-FTIR measurements were carried out on a Nicolet iS50 FT-IR spectrometer equipped with a liquid nitrogen-cooled MCT-A detector. The Si prism loaded with catalyst, platinum plate, and Ag/AgCl were used as the working electrode, counter electrode, and reference electrode, respectively. The 1 M KOH was used as electrolyte. In this work, catalysts suspensions were droped on the Au film modified Si prism. Before catalyst loading, the Au film was deposited directly on the Si prism by a

chemical deposition method. First, the Si prism was polished with a slurry of 100 nm Al_2O_3 and sonicated in acetone and deionized water. Next, the Si prism was soaked in a piranha solution (3:1 volumetric ratio of 98% H_2SO_4 and 30% H_2O_2) for 30 min and washed by deionized water for several times in order to removal organic contaminants. Following, the reflecting plane of the Si prism was dried with a nitrogen gas flow. Then, the reflecting surface was immersed in a mixture of the Au plating solution (5.75 mM $NaAuCl_4 \cdot 2H_2O$ + 0.025 M NH_4Cl + 0.075 M Na_2SO_3 + 0.025 M $Na_2S_2O_3$ + 0.026 M NaOH) and a 2 wt % HF solution at 60 for 5 min. After deposition, the Au film was rinsed with deionized water and dried by nitrogen gas flow. In situ ATR-FTIR spectra were recorded during stepping the working electrode potential.

Computational Details: All the calculations were implemented in the VASP package by employing density functional theory (DFT) with spin-polarized Perdew-Burke-Ernzerhof (PBE) exchange-correlation functional.[2,3] The cutoff energy of plane-wave basis set is 400 eV, and the (2×2×1), (2×3×1) and (3×3×1) grid sampling was used for Brillouin zone integration of CoS_2 (100), (110) and (111) slabs, respectively. The DFT+U method was adopted to describe the Co $3d$ electrons with an effective U value of 2 eV.[4,5] The convergence criteria of energy and force for structural optimization were set to 1×10^{-5} eV and 0.02 eV/Å, respectively. All the slabs were repeated periodically with a 20 Å vacuum layer between the images in the direction of the surface normal. The free energies of the reaction intermediates were obtained by $\Delta G = \Delta E_{ads} + \Delta ZPE - T\Delta S$, where ΔE_{ads} is the adsorption energy, ZPE is the zero point energy and S is the entropy at 298 K. The values of ($\Delta ZPE - T\Delta S$) were obtained through the post-processing tool for VASP code (VASPKIT).
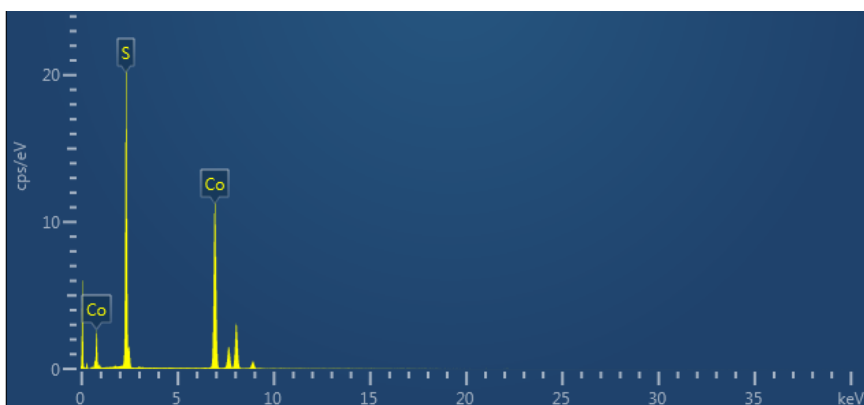
Element	k factor	wt%	wt% Sigma	Atomic %
S	0.991	48.36	0.12	66.24
Co	1.211	51.64	0.12	33.76
Total:		100.00		100.00

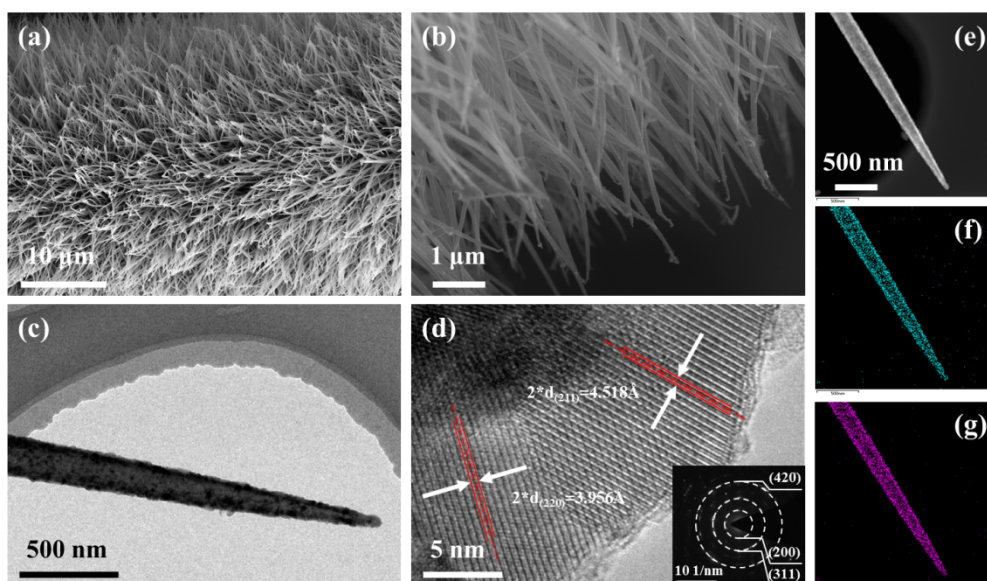**Fig. S1.** EDS spectrum and corresponding atomic ratio for CoS_2 OC.

Fig. S2. (a,b) SEM images of carbon paper@CoS$_2$ nanowire. (c) TEM image of one single CoS$_2$ nanowire. (d) HRTEM image of CoS$_2$ nanowire. Bottom-right inset in (d) is the corresponding SAED pattern. (e) STEM image and (f,g) corresponding element mappings of Co and S.

CoS$_2$ nanowire arrays (CoS$_2$ NW) on carbon paper (CC) were also fabricated for comparison by two-step hydrothermal reaction. **Fig. S2** shows the SEM, TEM, HRTEM, SEAD and EDS mapping of the CoS$_2$ NW sample. Clearly, the slim CoS$_2$ with pointed tips are homogeneously aligned on carbon paper, forming an uniform nanoarray on a large scale, as shown in **Fig. S2a** and **b**. The nanowire morphology was confirmed by TEM image (**Fig. S2c**). The single nanowire has porous and rough structure, composed of nanocrystallites with size of 10 to 20 nm. HRTEM image of the CoS$_2$ NW in **Fig. S2d** reveals well-resolved lattice distance of 2.259 and 1.978 Å, which are well corresponded to the (211) and (220) planes of cattierite-type CoS$_2$. **Fig. S2e-g** show the STEM image and corresponding EDS mapping of one CoS$_2$ NW, also presenting an uniform distribution of Co and S elements.
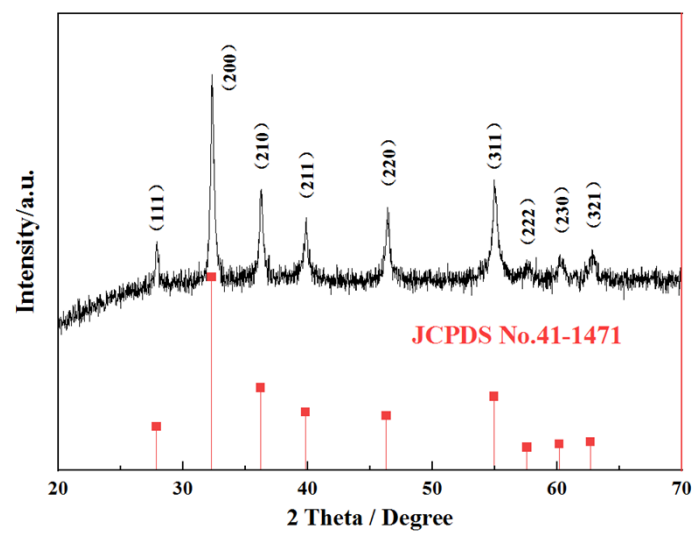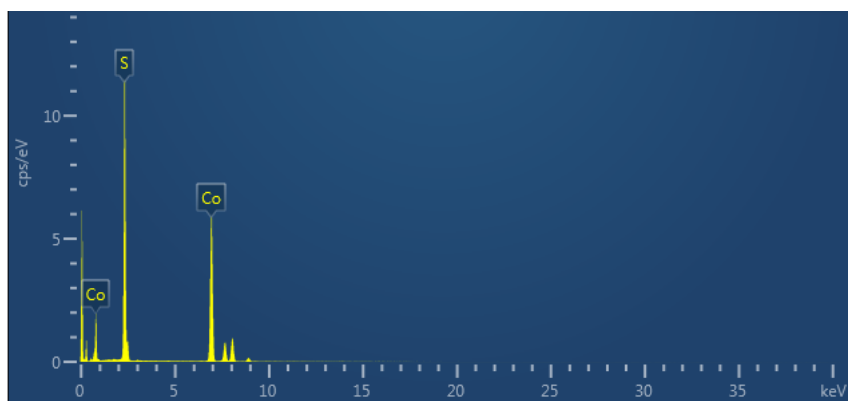
Fig. S3. XRD pattern of CoS$_2$ NW.

Element	k factor	wt%	wt% Sigma	Atomic %
S	0.991	50.10	0.12	64.86
Co	1.211	49.90	0.12	35.14
Total:		100.00		100.00

Fig. S4. EDS spectra of CoS_2 NW illustrating the presence of S and Co.
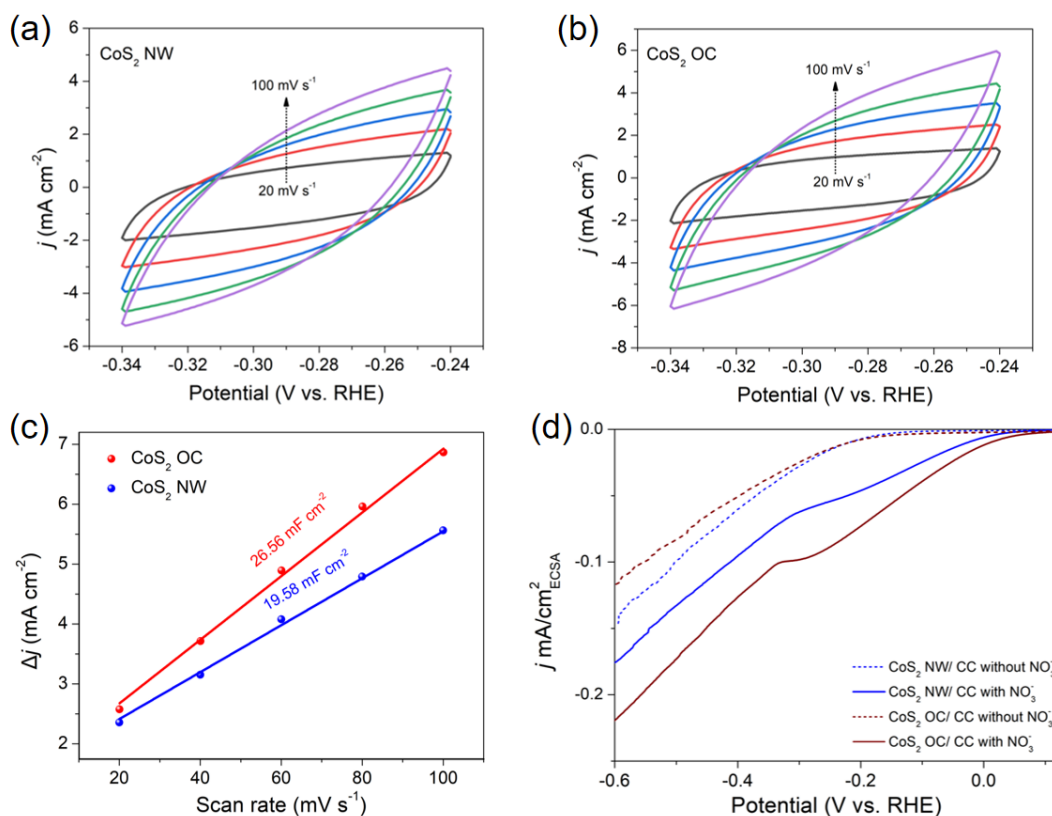
Fig. S5. CVs of (a) CoS_2 NW/CC and (b) CoS_2 OC/CC with various scan rates (20-100 mV s^{-1}). (c) The capacitive current densities as a function of scan rates for CoS_2 NW/CC and CoS_2 OC/CC. (d) ECSA-normalized LSV curves.

For the calculation of ECSA, 40 μF cm^{-2} is assumed as a moderate value of the specific capacitance for a flat surface. ECSA of the catalysts was calculated according to the following equation: ECSA $= C_{dl}/40$μF cm^{-2} per cm$^2_{ECSA}$. Our results show that the the current density of the octahedral CoS_2 nanocrystal (CoS_2 OC) is also significantly higher than that nanowire CoS_2 (CoS_2 NW) using ECSA approach when adding NO$_3^-$, **see** **Fig.** **S5.**
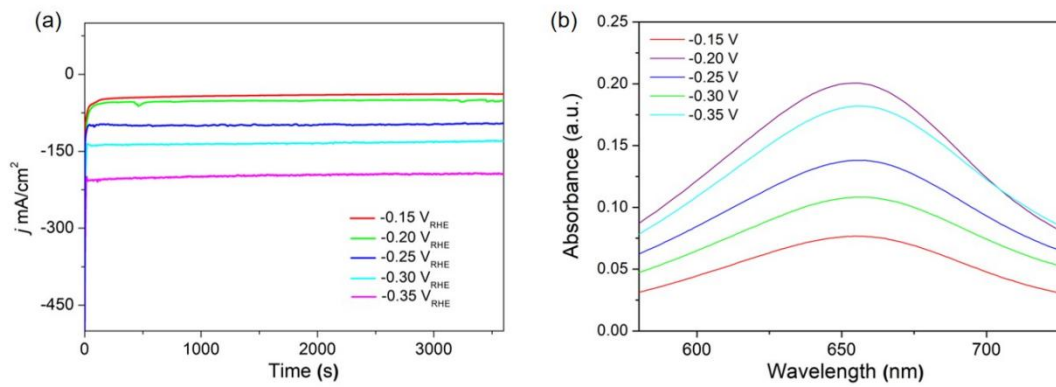
Fig. S6. (a) Chronoamperometry curves and (b) corresponding UV-Vis absorption spectra.
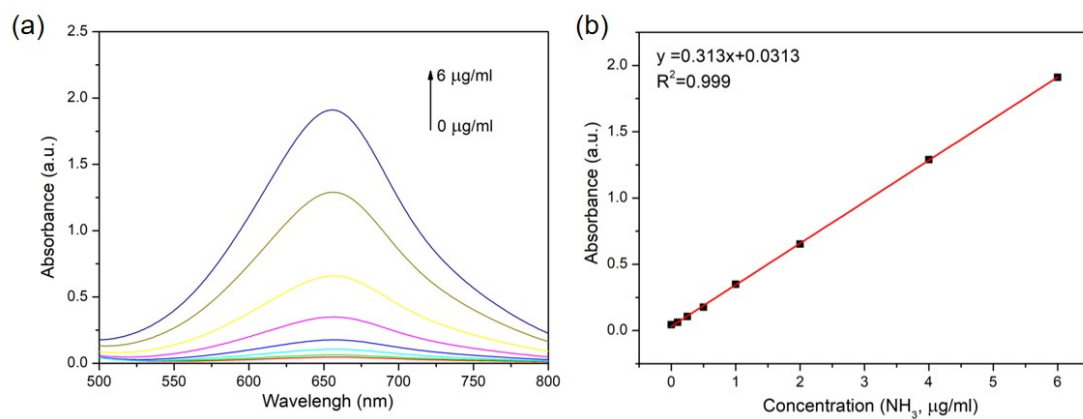
Fig. S7. (a) UV-vis absorption spectra of indophenol assays with NH_3 concentrations after incubated for 2 h at room temperature. (b) Calibration curve used for estimation of NH_3 concentration.
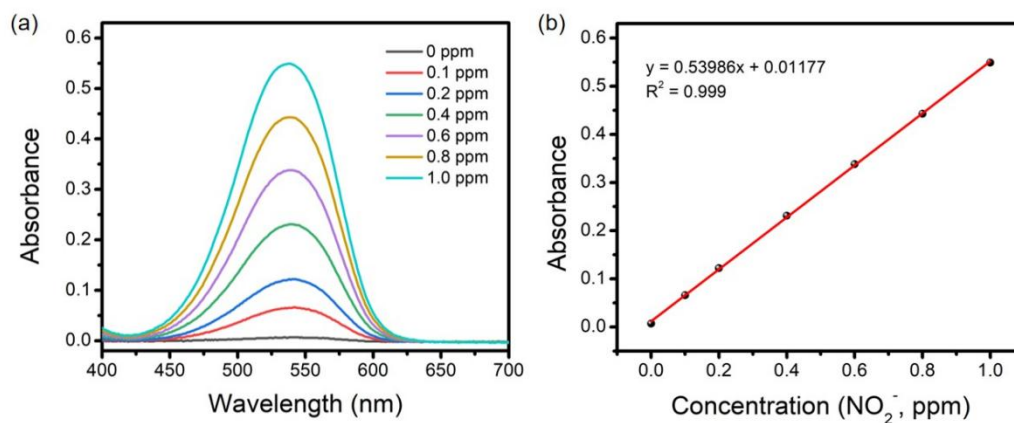
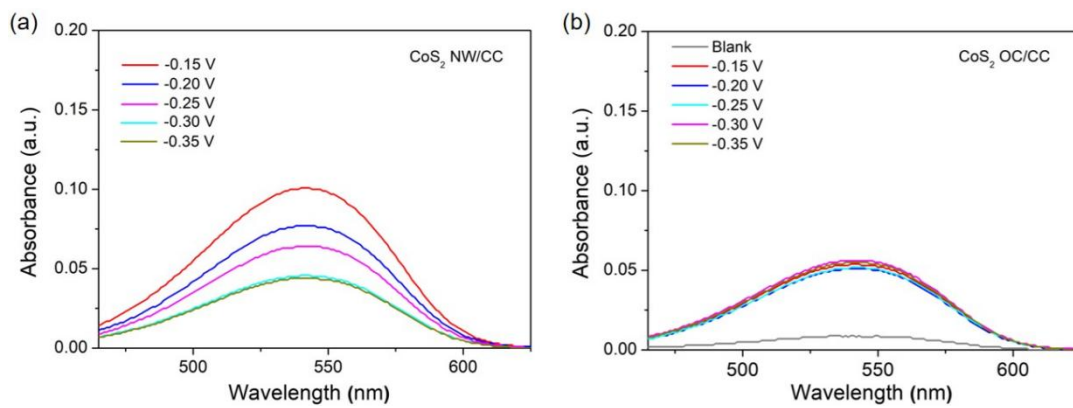**Fig. S8.** (a) UV-Vis absorption spectra of different NO_2^- concentrations after incubated for 15 min at room temperature. (b) Calibration curve used for estimation of NO_2^- concentration.

Fig. S9. (a,b) UV-Vis absorption spectrum of NO_2^- concentrations on CoS_2 NW/CC and CoS_2 OC/CC, respectively.
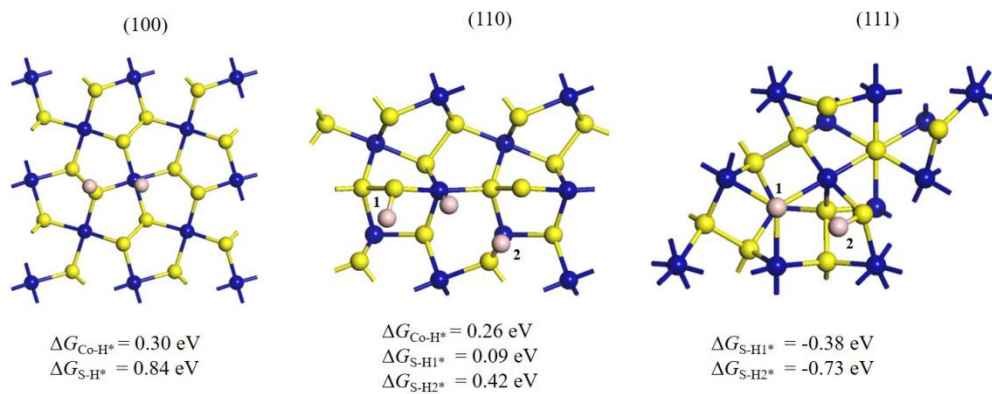
Fig. S10. Free energies of HER on CoS$_2$ (100), (110) and (111) surfaces. Co, blue; S, yellow; H, pink.
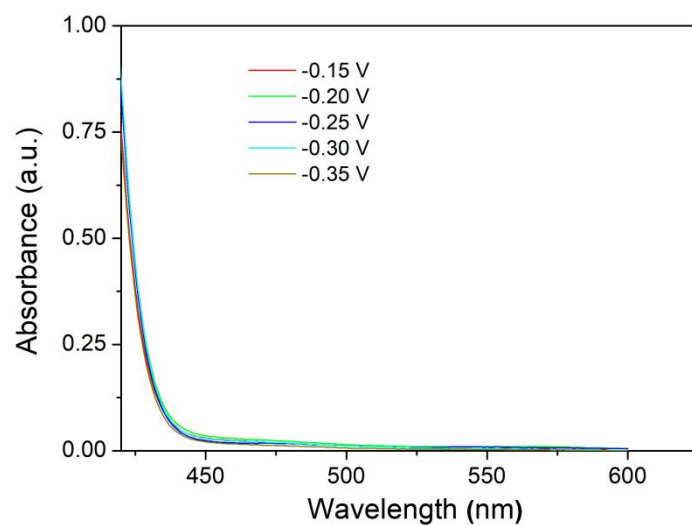
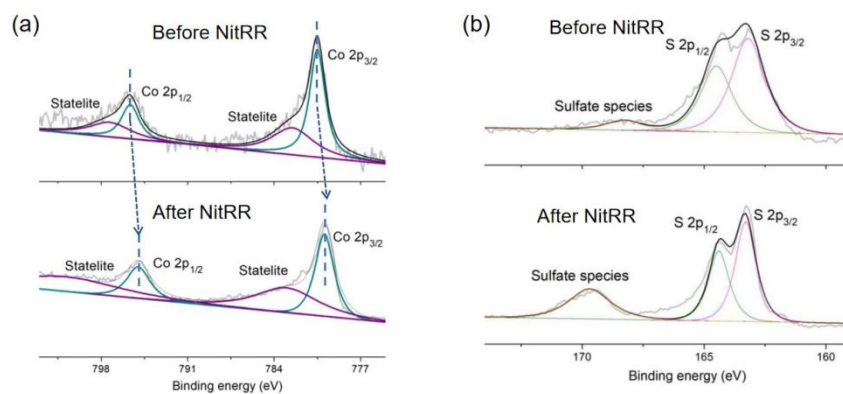**Fig. S11.** UV-Vis absorption spectrum at different electrode potentials after electrocatalysis for 1h.

Fig. S12. (a) XPS spectrum in Co 2p region before and after NO_3RR (b) XPS spectrum in S 2p region before and after NO_3RR.

Alternatively, the chemical state informations on CoS_2 OC/CC before and after NO_3RR were further confirmed by X-ray photoelectron spectroscopy (XPS). **Fig. S12a** shows that the two main peaks at 780.46 and 795.62 eV can be assigned to the characteristic peaks of Co $2p_{3/2}$ and Co $2p_{1/2}$, respectively, which can be ascribed to the Co^{2+}.[6,7] After NO_3RR, these two main peaks are slightly shifted to 779.98 and 795.11 eV, suggesting that a small amount of Co^{3+} appear. For S 2p, it exhibits binding energy located at 163.18, 164.44, and 168.5 eV, of which the first two can be ascribed to S $2p_{3/2}$ and S $2p_{1/2}$ peaks of Co-S bonds and last peak located at 168.5 eV might be ascribed to S-O bonding, see **Fig. S12b**.[6] After NO_3RR, the intensity of S-O bonding is obviously increased, suggesting that more oxygen-containing species is formed. Thus, it is inferred that the formation of Co^{3+} after NO_3RR could be attributed to the coverage of oxygen-containing species on catalyst surface due to its stronger electronegativity. Finally, Co^0 is not detectable by XPS in CoS_2 OC after NO_3RR, indicating that the CoS_2 OC catalyst is stability during reduction process.
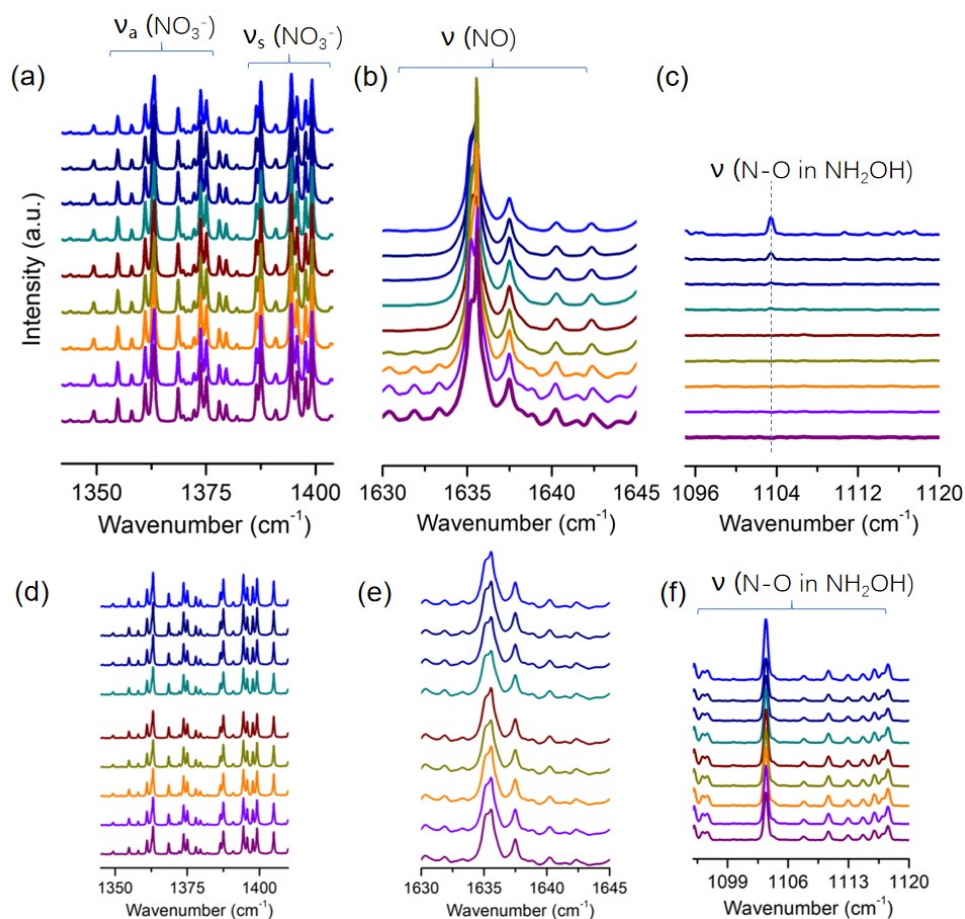
Fig. S13. In situ ATR-FTIR spectra of (a-c) CoS$_2$ OC and (d-f) CoS$_2$ NW.

The absorption bands at 1393 and 1364 cm^{-1} were ascribed respectively to N-O symmetric and asymmetric stretching vibration of NO$_3^-$,[8] see **Fig. S13a and d**. The absorption band of adsorbed *NO is detected at 1636 cm^{-1},[8] see **Fig. S13b and e**. **Fig. S13c** shows that on CoS$_2$ OC/CC the -N-O- stretching vibration of another hydroxylamine (NH$_2$OH) intermediate appears at lower electrode potential around 1110 cm^{-1} and then disappears as applied potential increases;[8] however, on CoS$_2$ NW/CC it has existed at all given electrode potentials, see **Fig. S13f**.
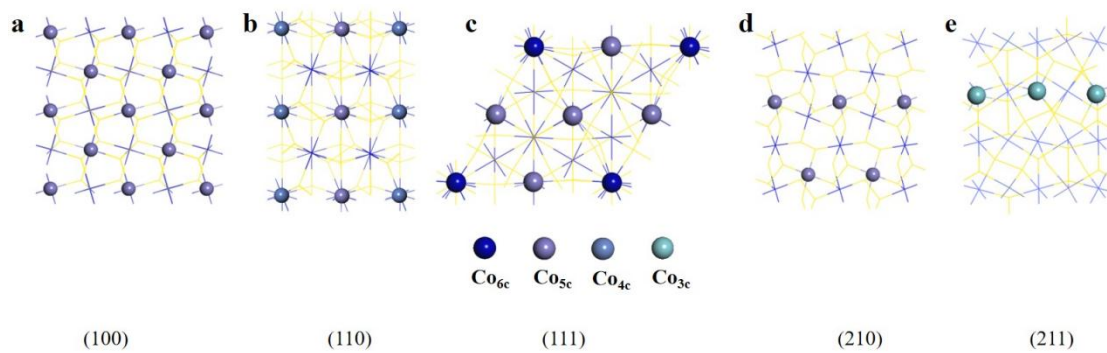
Fig. S14. The top view of atom configurations on CoS$_2$ (100), (110), (111), (210) and (211) surfaces, respectively.
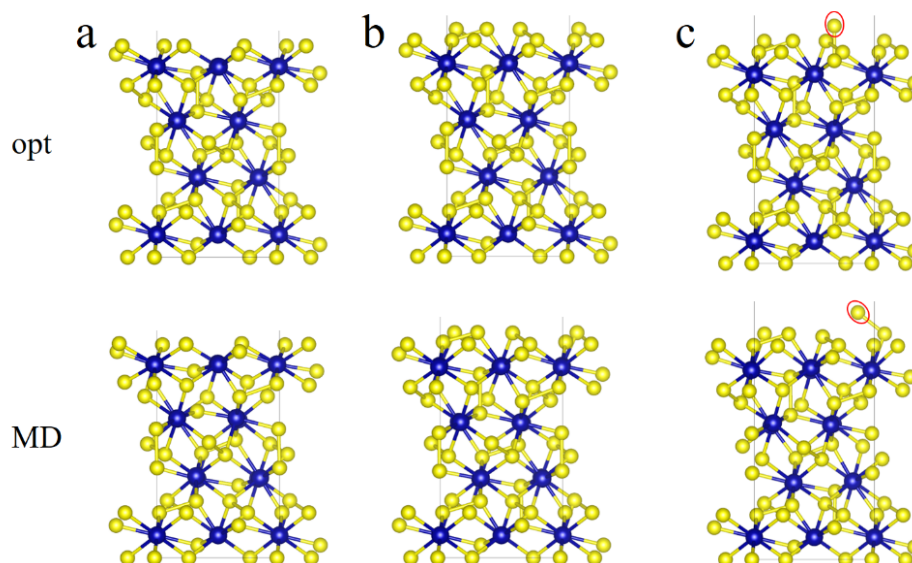
Fig. S15. The optimized and MD structures of (a) stoichiometry surface, (b) 3S surface and (c) 4S surface.

Two sulfur-rich surface models were checked for CoS_2 (111), namely (111)-3S and (111)-4S surfaces. We employed ab initio molecular dynamics (AIMD) to explore their stability under room temperature. After 10 ps simulation at 300K, atomic structures of stoichiometry and 3S surfaces underwent very tiny changes, which means that stoichiometry and 3S surfaces are reasonably stable at room temperature (**Fig. S15**). Notably, there is a reconstruction of S atoms on 4S surfaces, see **Fig. S15c**.
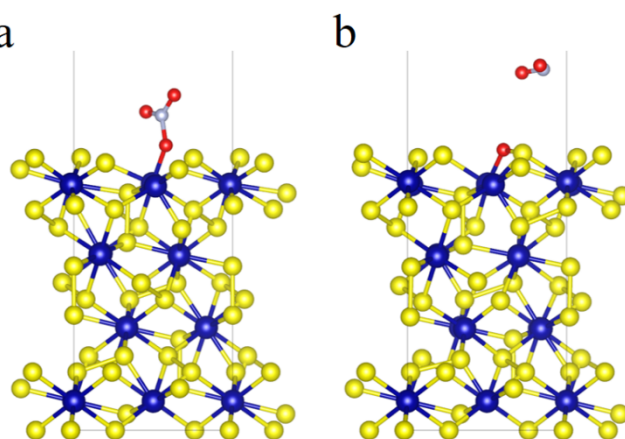
Fig. S16. AIMD structures of NO_3^* on CoS_2 (111) stoichiometry facets, (a) 0 *ps*, (b) 0.4 ps.

When the NO_3^* molecule was placed at a high height from the (111) stoichiometry facet, it could not dissociate during geometry optimization (**Fig. S16**a). However, the NO_3^* molecule would spontaneously dissociate during the AIMD simulation at 300K, which the NO_3^* molecule would dissociate into O* and NO_2 within 0.4 ps (**Fig. S16b**) meaning a metastable state. We have further employed CI-NEB method to identify saddle-point structures for the NO_3^* --> $NO^* + 2O^*$ dissociation steps. The barriers of NO_3^* --> $O^* + NO_2^*$ and NO_2^* --> $O^* + NO^*$ on CoS_2 (111) stoichiometry facets are 0.24 eV and 0.25 eV, respectively (**Fig. S17a** and **Fig. S18**), meaning that the NO_3^* --> $NO^* + 2O^*$ dissociation steps could occur under room temperature. However, the barrier of NO_3^* --> $O^* + NO_2^*$ on (111)-3S facet is 0.18 eV, and the NO_2^* --> $O^* + NO_{(g)}$ is higher barrier with 0.93 eV (**Fig. S17b** and **Fig. S19**). It suggests that the CoS_2 (111) stoichiometry facet is the actual catalytic surface due to the lower activation energy from *NO_2 to *O +*NO.
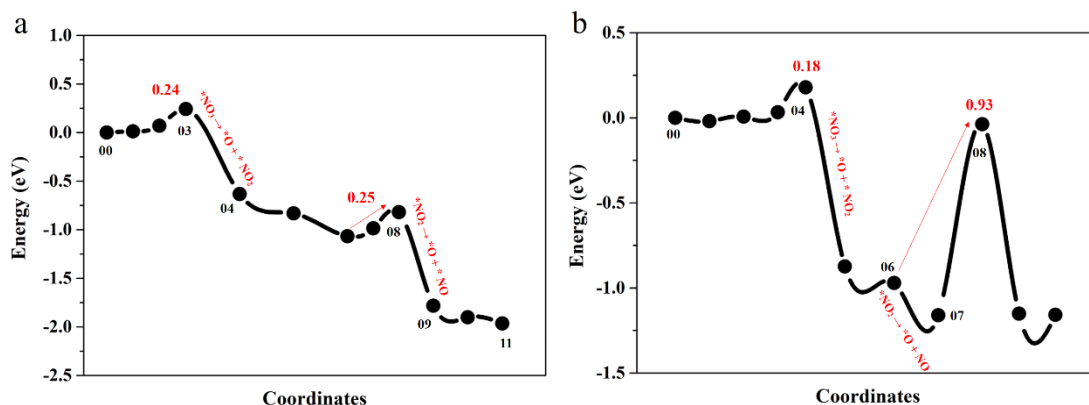

Fig. S17. Calculated energy profile of NO_3^* --> $NO^* + 2O^*$ on (111) facets, (a)

stoichiometry CoS_2, (b) (111)-3S surface.

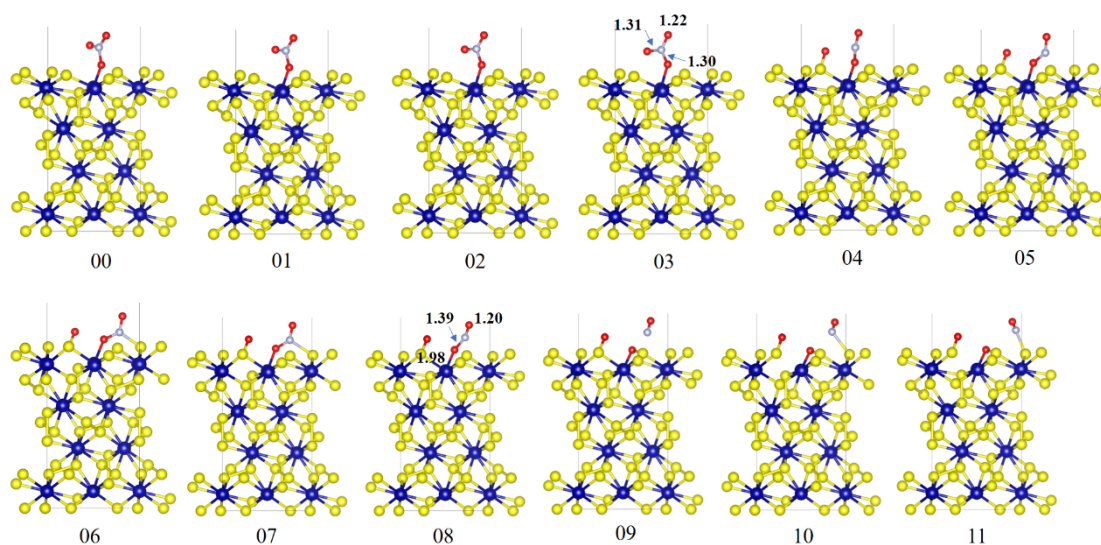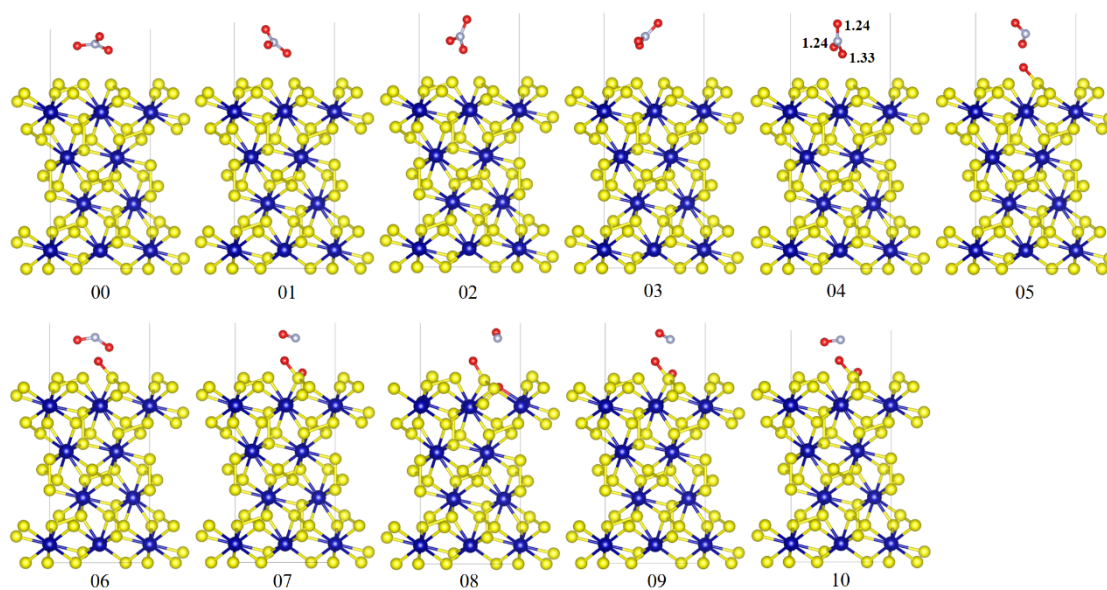**Fig. S18.** The corresponding structures of $NO_3^* \longrightarrow NO^* + 2O^*$ steps on (111) stoichiometry CoS_2.

Fig. S19. The corresponding structures of $NO_3^* \longrightarrow NO^* + 2O^*$ steps on (111)-3S surface.

The dissociation barriers of NO_3^* on (110) and (100) surfaces have been calculated, see **Fig. S20-22**. The barriers of NO_3^* --> $O^* + NO_2^*$ on (110) and (100) surfaces are 2.06 and 1.34 eV (**Fig. S20-22**), respectively, which means that the NO_3^* --> $O^* + NO_2^*$ steps are hard to occur on these two surfaces. Hence, the study of subsequent NO_2^* --> $O^* + NO^*$ steps has been omitted.

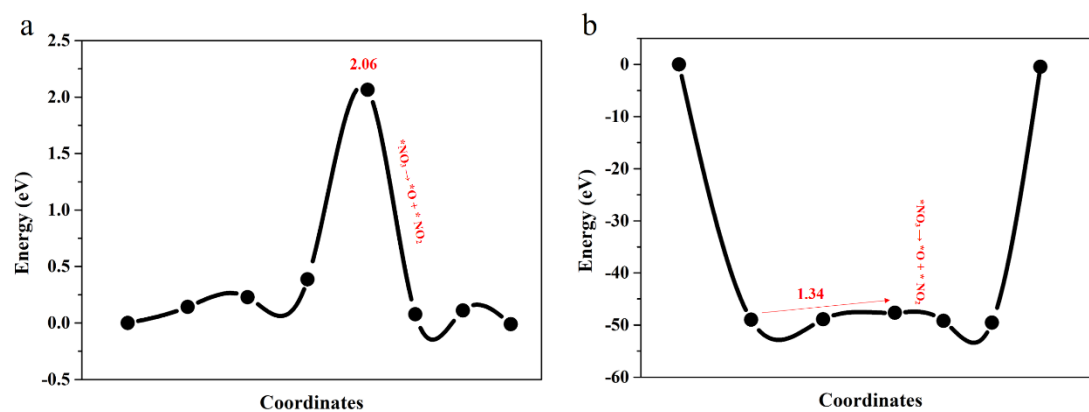**Fig. S20.** Calculated energy profile of NO_3^* dissociation of (a) (110) surface and (b) (100) surface.
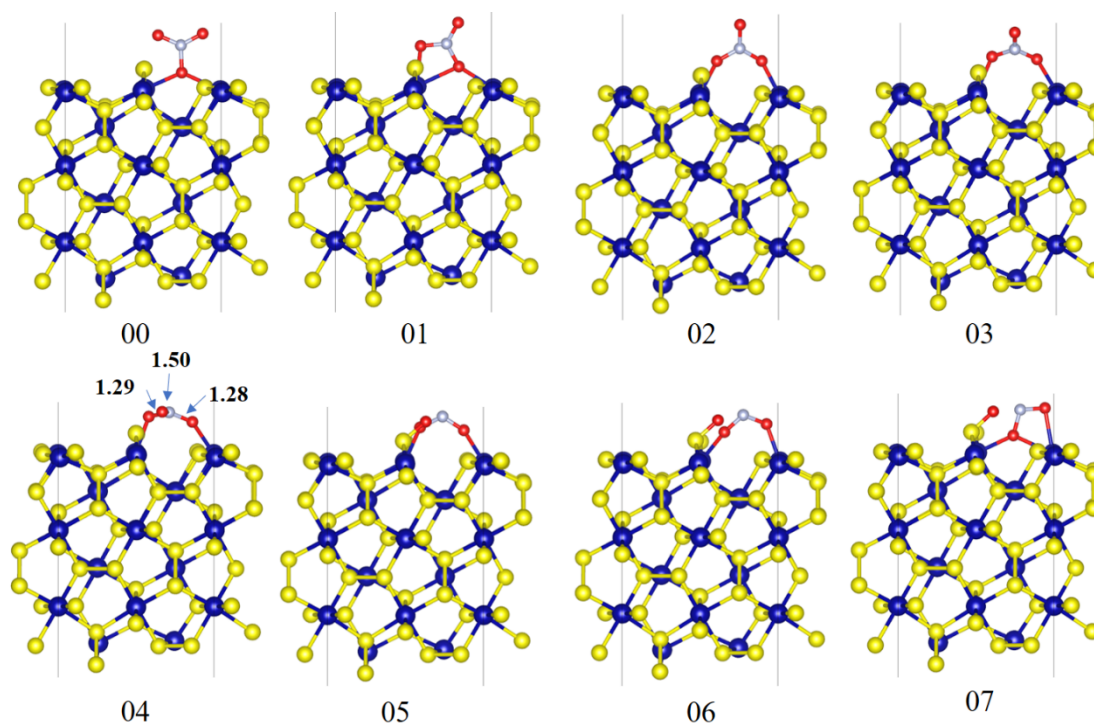
Fig. S21. The corresponding structures of NO_3^* dissociation on (110) surface.
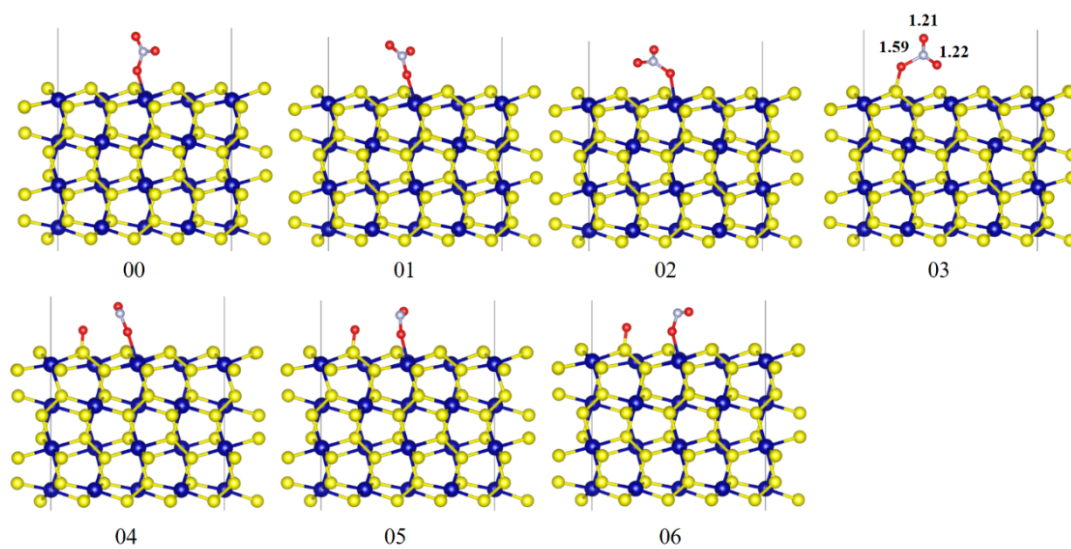
Fig. S22. The corresponding structures of NO_3^* dissociation on (100) surface.

(100)
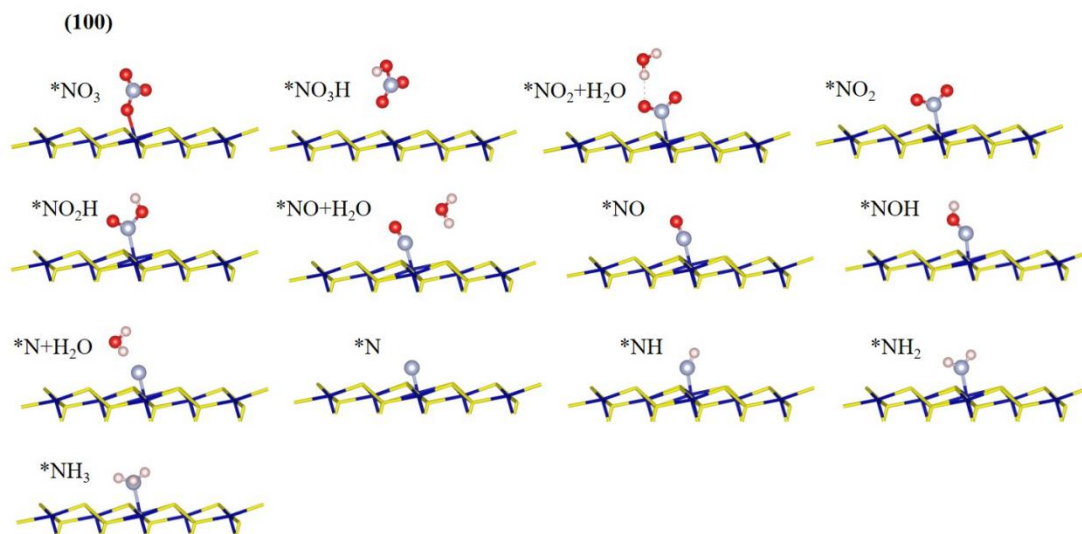
Fig. S23. The atom configurations of NO_3RR process on CoS_2 (100) surface. Co, blue; S, yellow; H, pink; N, grey; O, red.

(110)

*NO$_3$ *NO$_3$H   *NO$_2$+H$_2$O   *NO$_2$ *NO$_2$H

*NO+H$_2$O   *NO   *NOH   *N+H$_2$O   *N

*NH   *NH$_2$ *NH$_3$
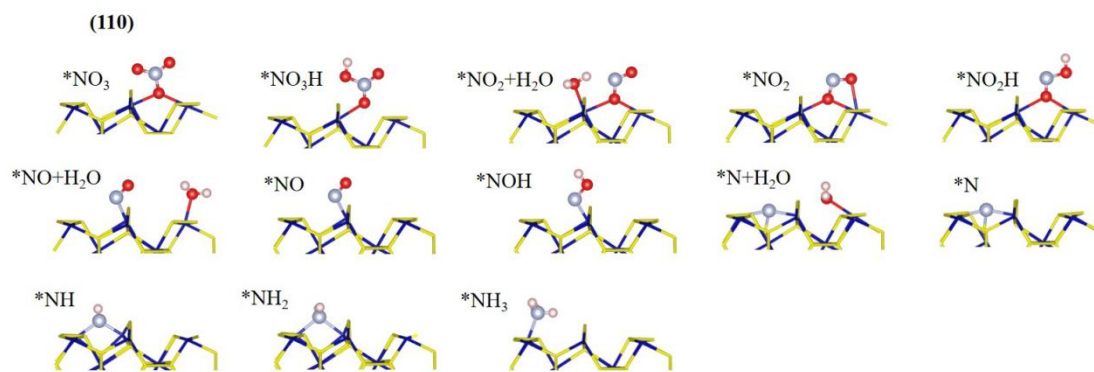
Fig. S24. The atom configurations of NO$_3$RR process on CoS$_2$ (110) surface.

(111)

*NO+2*O   *NO+*O+*OH   *NO+*O+H_2O *NO+*O   *NO+*OH

*NO+H_2O *NO   *NOH   *N+H_2O *N

*NH   *NH$_2$ *NH$_3$
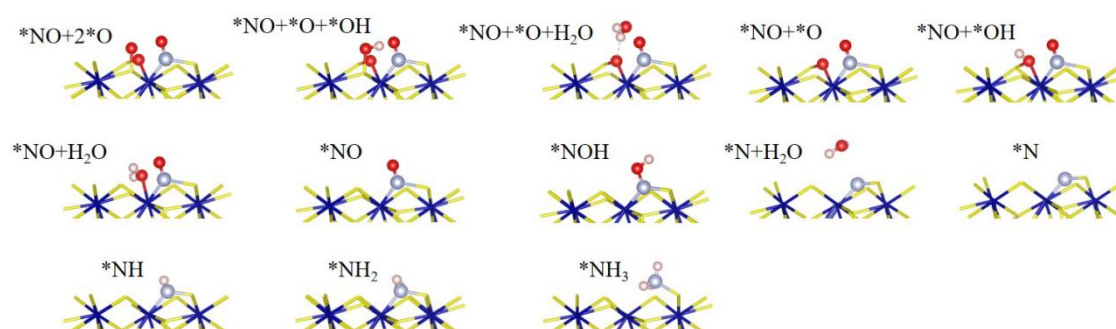
Fig. S25. The atom configurations of NO_3RR process on CoS_2 (111) surface.

V_{2c} V_{3c}
$\Delta E = 0$ $\Delta E = 0.86$
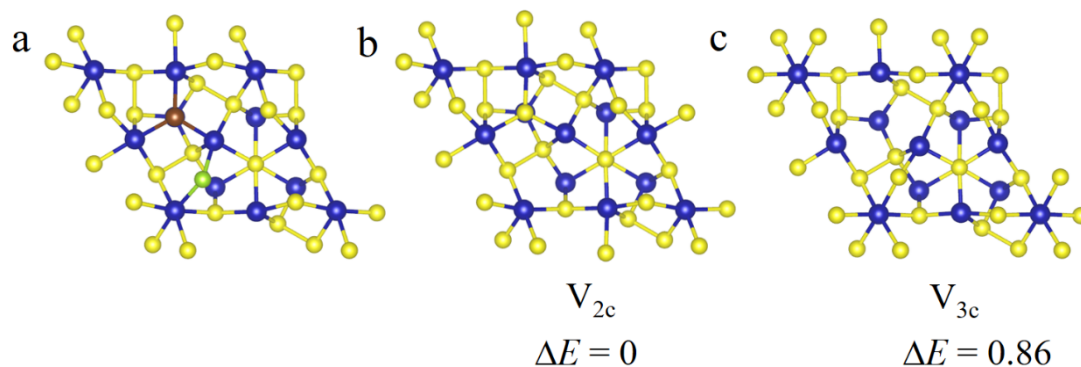
Fig. S26. The optimized structures of (111) facets, (a) stoichiometry, (b) V_{2c}, (b) V_{3c}. The green and brown atoms are two-coordinated and three-coordinated S atoms, respectively.

The (111) stoichiometry facets were selected to study defect impact on NO_3RR reaction. There exit two-coordinated and three-coordinated S atoms on (111) stoichiometry facets, which corresponding defects are designated as V_{2c} and V_{3c}. The V_{2c} is more easily formed than V_{3c} (Fig. S26) due to the lower formation energy (ΔE). The NO_3* molecule on the (111)-V_{2c} facets still did not dissociate after a 10 ps simulation at 300K (Fig. S27), indicating that S defects are not conducive to the dissociation of the NO_3* molecule. However, on the CoS_2(111) surface without S defects, the NO_3 molecule has already spontaneously dissociated. Our in situ Raman and infrared spectroscopy results show that surface NO_3* is readily converted. Therefore, we are inclined to believe that the Co active sites without S defects are the primary catalytic sites in our material.

Subsequently, the reaction free energy (ΔG) is also calculated to identify the rate-determining step (RDS). As for (111)-V_{2c} facets with S vacancy (Fig. S28), the first hydrogenation step (*$NO_3 \rightarrow$ *NO_3H) is the RDS with $\Delta G = 0.44$ eV, and this ΔG value is smaller than that of (111) stoichiometry facets. So, it indicates that preparing CoS_2 catalyst with S vacancies could also be a promising material for NO_3RR.
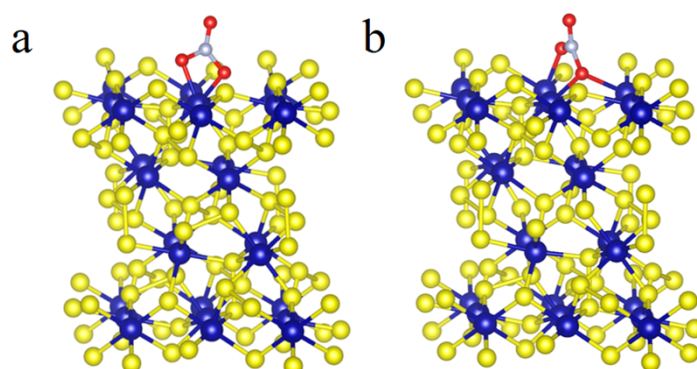
Fig. S27. AIMD structures of NO_3* on (111)-V_{2c} facets, (a) 0 *ps*, (b) 10 *ps*.
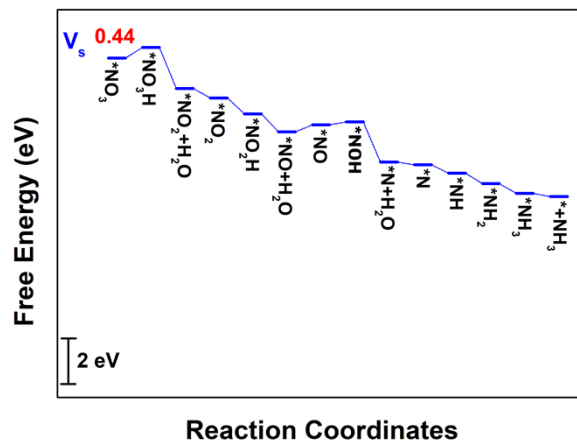
Fig. S28. Free energy diagrams of NO$_3$RR reaction on (111)-V$_{2c}$ facets.

| 6 h | 10 h |
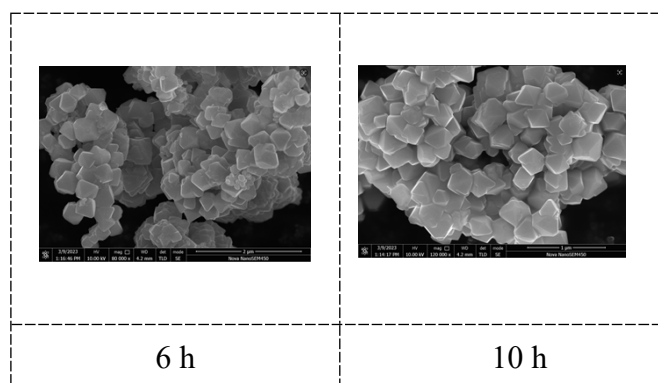
Fig. S29. The morphological changes of CoS_2 OC after different electrolysis times for NO_3RR.

We found that CoS_2 OC exhibits partial agglomeration (Fig. S29), but its performance remains stable. This suggests that the CoS_2 OC may have some resistance to agglomeration or that agglomeration has little impact on its performance.

Table S1. Comparison of the catalytic performances of CoS$_2$ OC with reported Co-based NO$_3$RR catalysts at ambient conditions.

| Catalyst	Electrolyte	NH$_3$ yield rate (μmol h^{-1} cm^{-2}@V vs. RHE)	FE (%@V vs. RHE)	Ref.
CoS$_2$ OC	1 M KOH (0.1 M NO$_3^-$)	588 @ -0.35V	97.5 @ -0.25V	This work
Co@TiO$_2$/TP	0.1 M PBS (0.1 M NO$_3^-$)	800 @ -0.40V	96.7 @ -0.70V	[9]
Co-P/TP	0.2 M PBS (200 ppm NO$_3^-$)	24.47 @ -0.6	93.6 @ -0.3	[10]
Co$_2$AlO$_4$/CC	0.1 M PBS (0.1 M NO$_3^-$)	464.7 @ -0.9	92.6 @ -0.7	[11]
Co/CoO NSA	0.1 M Na$_2$SO$_4$ (200 ppm NO$_3^-$)	194.46 @ -0.65	93.8 @ -0.65	[12]
ZnCo$_2$O$_4$ NSA/CC	0.1 M NaOH (0.1 M NO$_3^-$)	634.74 @ -0.8	98.33 @ -0.6	[13]
CoTiO$_{3-x}$/CP	1 M KOH (0.1 M NO$_3^-$)	858 @ -1.0	92.6 @ -1.0	[14]
NiCo$_2$O$_4$/CC	0.1 M NaOH (0.1 M NO$_3^-$)	973.2 @ -0.6	99 @ -0.3	[15]
CoP NAs/CFC	1 M NaOH (1 M NO$_3^-$)	956 @ -0.3	100 @ -0.3	[16]
CuCo	1 M KOH (0.1 M NO$_3^-$)	4800 @ -0.2	100 @ -0.2	[8]
Mn-Co$_3$O$_4$	0.5 M K$_2$SO$_4$ (0.1 M NO$_3^-$)	2058 @ -1.2	99.5 @ -1.2	[17]
Fe$_3$C NPs@NCF	0.1 M NaOH (0.1 M NO$_3^-$)	466 @ -0.8	96.9 @ -0.8	[18]
Cu nanosheets	0.1 M KOH (10 mM KNO$_3$)	21.67 @ -0.15 V	99.7 @ -0.15 V	[19]

$FeCo_2O_4$	0.1 M NaOH (20 mM $NaNO_3$)	277.1 @ -0.5V	95.9	[20]
$Cu_{50}Ni_{50}$	1 M KOH (100 mM NO_3^-)	80.7 @ -0.15	82.0 @ -0.15	[21]
Fe_3O_4/PC	0.1 M NaOH (0.1 M NO_3^-)	394.8 @ -0.4	91.6 @ -0.4	[22]

REFERENCES

[1]   G. W. Watt and J. D. Chrisp, Spectrophotometric method for determination of hydrazine, *Anal. Chem.,* 1952, **24**, 2006.

[2]   G. Kresse and J. Furthmüller, Efficiency of ab-initio total energy calculations for metals and semiconductors using a plane-wave basis set, *Comp. Mater. Sci.,* 1996, **6**, 15.

[3]   G. Kresse and J. Furthmüller, Efficient iterative schemes for ab initio total-energy calculations using a plane-wave basis set, *Phys. Rev. B,* 1996, **54**, 11169.

[4]   S. Li, Y. Zhang and X. Niu, Defects and impurities induced structural and electronic changes in pyrite CoS_2: first principles studies, *Phys. Chem. Chem. Phys.,* 2018, **20**, 11649.

[5]   A. Rohrbach, J. Hafner and G. Kresse, Electronic correlation effects in transition-metal sulfides. *Journal of Physics: Condensed Matter*, 2003, **15**, 979.

[6]   P. Chen, T. Zhou, M. Chen, Y, Tong, N, Zhang, X. Peng, W. Chu, X. Wu, C. Wu and Y. Xie, Enhanced catalytic activity in nitrogen-anion modified metallic cobalt disulfide porous nanowire arrays for hydrogen evolution, *ACS Catal.,* 2017, **7**, 7405.

[7]   P. Chen, N. Zhang, S. Wang, T. Zhou, Y. Tong, C. Ao, W. Yan, L. Zhang, W. Chu, C.Wu and Y. Xie, Interfacial engineering of cobalt sulfide/graphene hybrids for highly efficient ammonia electrosynthesis, *P. Natl. Acad. Sci. USA,* 2019, **116**, 6635.

[8]   J. Fang, Q. Zheng, Y. Lou, K. Zhao, S. Hu, G. Li, O. Akdim, X. Huang and S. Sun, Ampere-level current density ammonia electrochemical synthesis using CuCo

nanosheets simulating nitrite reductase bifunctional nature, *Nat. Commun.,* 2022, **13**, 7899.

[9] X. Fan, D. Zhao, Z. Deng, L. Zhang, J. Li, Z. Li, S. Sun, Y. Luo, D. Zheng, Y. Wang, B. Ying, J. Zhang, A. A. Alshehri, Y. Lin, C. Tang, X. Sun and Y. Zheng, Constructing $Co@TiO_2$ nanoarray heterostructure with schottky contact for selective electrocatalytic nitrate reduction to ammonia, *Small,* 2023, **19**, 2208036.

[10] Z. Li, G. Wen, J. Liang, T. Li, Y. Luo, Q. Kong, X. Shi, A. M. Asiri, Q. Liu and X. Sun, High-efficiency nitrate electroreduction to ammonia on electrodeposited cobalt﹣phosphorus alloy film, *Chem. Commun.,* 2021, **57**, 9720.

[11] Z. Deng, J. Liang, Q. Liu, C. Ma, L. Xie, L. Yue, Y. Ren, T. Li, Y. Luo, N. Li, B. Tang, A. A. Alshehri, I. Shakir, P. O. Agboola, S. Yan, B. Zheng, J. Du, Q. Kong and X. Sun, High-efficiency ammonia electrosynthesis on self-supported Co_2AlO_4 nanoarray in neutral media by selective reduction of nitrate, *Chem. Eng. J.,* 2020, **435**, 135104.

[12] Y. Yu, C. Wang, Y. Yu, Y. Wang and B. Zhang, Promoting selective electroreduction of nitrates to ammonia over electron-deficient Co modulated by rectifying Schottky contacts, *Sci. China Chem.,* 2020, **63**, 1469.

[13] Z. Li, J. Liang, Q. Liu, L. Xie, L. Zhang, Y. Ren, L. Yue, N. Li, B. Tang, A. A. Alshehri, M. S. Hamdy, Y. Luo, Q. Kong and X. Sun, High-efficiency ammonia electrosynthesis via selective reduction of nitrate on $ZnCo_2O_4$ nanosheet array, *Mater. Today Phy.,* 2022, **23**, 100619.

[14] X. Fan, J. Liang, L. Zhang, D. Zhao, L. Yue, Y. Luo, Q. Liu, L. Xie, N. Li, B. Tang, Q. Kong and X. Sun, Enhanced electrocatalytic nitrate reduction to ammonia using plasma-induced oxygen vacancies in $CoTiO_{3-x}$ nanofiber, *Carbon Neutralization,* 2022, **1**, 6.

[15] Q. Liu, L. Xie, J. Liang, Y. Ren, Y. Wang, L. Zhang, L. Yue, T. Li, Y. Luo, N. Li, B. Tang, Y. Liu, S. Gao, A. A. Alshehri, I. Shakir, P. O. Agboola, Q. Kong, Q. Wang, D. Ma and X. Sun, Ambient Ammonia Synthesis via Electrochemical

Reduction of Nitrate Enabled by $NiCo_2O_4$ Nanowire Array, *Small,* 2022, **18**, 2106961.

[16] S. Ye, Z. Chen, G. Zhang, W. Chen, C. Peng, X. Yang, L. Zheng, Y. Li, X. Ren, H. Cao, D. Xue, J. Qiu, Q. Zhang and J. Liu, Elucidating the activity, mechanism and application of selective electrosynthesis of ammonia from nitrate on cobalt phosphide, *Energy Environ. Sci.,* 2022, **15**, 760.

[17] D. Liu, L. Qiao, Y. Chen, P. Zhou, J. Feng, C. C. Leong, K. W. Ng, S. Peng, S. Wang, W. F. Ip and H. Pan, Electrocatalytic reduction of nitrate to ammonia on low-cost manganese-incorporated Co_3O_4 nanotubes, *Appl. Catal., B,* 2023, **324**, 122293.

[18] X. Liu, T. Xie, Z. Cai, Z. Li, L. Zhang, X. Fan, D. Zhao, S. Sun, Y. Luo, Q. Liu, and X. Sun, Fe_3C nanoparticles decorated 3D nitrogen-doped carbon foam as a highly efficient electrocatalyst for nitrate reduction to ammonia. *J. Electroanal. Chem.*, 2023, **933**, 117295.

[19] X. Fu, X. Zhao, X. Hu, K. He, Y. Yu, T. Li, Q. Tu, X. Qian, Q. Yue, M. R. Wasielewski, Y. Kang, Alternative route for electrochemical ammonia synthesis by reduction of nitrate on copper nanosheets. *Appl. Mater. Today*, 2020, *19*, 100620.

[20] J. Li, D. Zhao, L. Zhang, L. Yue, Y. Luo, Q. Liu, N. Li, A. A. Alshehri, M. S. Hamdy, Q. Li, X. Sun, A $FeCo_2O_4$ nanowire array enabled electrochemical nitrate conversion to ammonia. *Chem. Commun.*, **2022**, 58, 4480-4483.

[21] Y. Wang, A. Xu, Z. Wang, L. Huang, J. Li, F. Li, J. Wicks, M. Luo, D. Nam, C. Tan, Y. Ding, J. Wu, Y. Lum, C. Dinh, D. Sinton, G. Zheng and E. Sargent, Enhanced nitrate-to-ammonia activity on copper-nickel alloys via tuning of intermediate adsorption. J. Am. Chem. Soc., 2020, 142, 5702-5708.

[22] T. Xie, Z. Cai, X. Liu, J. Li, X. Fan, X. He, Y. Luo, D. Zheng, S, Sun, S. Alfaifi, C. Xu, X. Sun, Fe_3O_4 nanoparticle-decorated 3D pinewood-derived carbon for high-efficiency electrochemical nitrate reduction to ammonia. *Chem. Commun.*, 2023, 59, 12322-12325.